BIBECHANA
Vol. 23, No. 2, April 2026, 157-168

ISSN 2091-0762 (Print), 2382-5340 (Online)
Journal homepage: http://nepjol.info/index.php/BIBECHANA
Publisher:Dept. of Phys., Mahendra Morang A. M. Campus (Tribhuvan University)Biratnagar

Elucidation of nanoscale features and antimicrobial activity of *Yashad* and *Vanga Bhasmas*

Bimal Rajchal[1,2,3,4], Yub Narayan Thapa[1,3,4,5], Deepshikha Karki[1,3,4], Pramod Bhatta[6], Motee Lal Sharma[1,7], Vimal Katiyar[8*], Rameshwar Adhikari[1,3,4,8*]

[1]*Central Department of Chemistry, Tribhuvan University, Kirtipur, Nepal.*
[2]*Bhaktapur Multiple Campus, Tribhuvan University, Bhaktapur, Nepal.*
[3]*Nepal Polymer Institute (NPI), Kathmandu, Nepal.*
[4]*Research Centre for Applied Science and Technology, Tribhuvan University, Kirtipur, Nepal.*
[5]*Tribhuvan Multiple Campus, Tribhuvan University, Tansen, Palpa, Nepal.*
[6]*Vidushi Yogmaya Himalayan Ayurveda University, Sankhuwasabha, Nepal.*
[7]*Nepal Academy of Science and Technology (NAST), Lalitpur, Nepal.*
[8]*Department of Chemical Engineering, Indian Institute of Technology Guwahati, Assam, India.*

*Corresponding authors: Email: vkatiyar@iitg.ac.in;nepalpolymer@yahoo.com

Abstract

Yashad Bhasma (YB) and Vanga Bhasma (VB) are traditional Ayurvedic zinc–based and tin-based formulations, respectively, enriched with therapeutic values. Despite their long history, their scientific validation, physicochemical features, and antimicrobial activity are, however, less explored. This study aims to prepare these Bhasmas by following the traditional method described in the Ayurvedic text "Rasashastra" and evaluating their physicochemical and antimicrobial features. Ultraviolet-visible spectroscopy (UV–vis), Fourier transform infrared spectroscopy (FTIR), X–ray diffraction (XRD), Raman spectroscopy, Scanning electron microscopy coupled with energy dispersive X-ray analysis (SEM–EDX), and Transmission electron microscopy (TEM) were used to evaluate the physicochemical and morphological features. The analyses confirmed the crystalline wurtzite zinc oxide structures of YB agglomerated in a circular fashion with an average particle size distribution of 21.3 nm and rutile tin oxide structures of VB agglomerated in flower–like fashion with an average particle size distribution of 38.5 nm. The antimicrobial activity of both Bhasmas was evaluated against wound pathogens B. subtilis and S. epidermidis using the agar well diffusion method. The macro-broth dilution method was used to assess their minimum inhibitory concentration (MIC) and minimum bactericidal concentration (MBC). YB showed 11.00 ± 0.3 *mm and* 11.34 ± 0.3 *mm zone of inhibition (ZOI) against B. subtilis and S. epidermidis, respectively and MBC of* $12.5 - 25$ *mg* $m.L^{-1}$ *against both pathogens. The findings provide evidence for the nanoscale features and antimicrobial potential of Ayurvedic Bhasmas, supporting their therapeutic values.*

Keywords
Ayurvedic Bhasmas, Zinc calx, Tin calx, *Bhasmikaran*, Herbo–metallic formulations.

Article information
Manuscript received: February 3, 2026; Revised: April 17, 2026; Accepted: April 21, 2026
DOI https://doi.org/10.3126/bibechana.v23i2.92663

1 Introduction

Ayurvedic Bhasmas are ultrafine and highly refined residue produced through an intricate alchemical and pharmaceutical process involving the purification, trituration and incineration of metals, minerals, gemstones or substances of animal origin. These are traditionally regarded as smooth, non–toxic, and biocompatible Ayurvedic formulations, enriched with essential trace metal elements such as zinc, copper and iron, aimed to manage a wide range of human ailments [1–3]. These attributes have been supported by several experimental toxicological studies conducted under controlled conditions [4–6]. *Yashad* and *Vanga Bhasma* are two metal-based *Bhasmas* that hold broad and significant medicinal value in Ayurvedic healthcare. *Yashad Bhasma*, obtained by processing of elemental zinc, is specifically prescribed for diabetes, skin ailments, and immune-related disorders [7–10], while *Vanga Bhasma*, derived from elemental tin, is prescribed for genital disorders, urinary problems, and respiratory ailments [10–13]. These *Bhasmas*, containing nano– or micro–scale level metal oxide or metal sulphide particles, also demonstrate significant antimicrobial properties and hold potential applications in biomedical sectors [14–16].

The preparation method of *Ayurvedic Bhasmas*, known as "*Bhasmikaran*", relies on manual labour, simplified tools and traditional practices. Classical Ayurvedic treatises like *Rasa Ratna Samuccaya*, *Rasa Tarangini*, *Rasashastra*, and *Bhaishajya Ratnawali* describe complex pharmaceutical processing techniques such as *Shodhana* (purification), *Bhavana* (impregnation), *Marana* (incineration), *Jarana* (roasting), *Mardana* (grinding), *Sandhana* (fermentation) and *Amritikarana* (immortalization) to transform metals, minerals, gemstones, and animal-derived substances into extremely fine, smooth, highly absorbable, therapeutically potent, and non-toxic forms called *Bhasmas* [17–19]. Each of these techniques utilizes particular tools, fuels, media, and methods, many of which closely resemble top-down nanofabrication techniques like chemical etching, plasma treatment, mechanical milling, laser ablation, and lithography [20, 21].

The increasing public interest in traditional medicine in recent years has intensified the demand for research in Ayurvedic healthcare. The discovery that *Ayurvedic Bhasmas* possess inherent nanoscale properties has drawn attention to these ancient methods as early forms of top-down nanofabrication, highlighting their relevance in the field of nanotechnology and pharmaceutical sciences [22, 23]. Despite a long history of empirical use and therapeutic success, the scientific understanding of *Bhasmas*, particularly their structure, physicochemical properties, formation mechanisms, and functional attributes, remains less explored within the scientific community. Therefore, researchers are interested in exploring integrative and innovative applications of these formulations across diverse health care sectors. It helps enhance our understanding of these traditional formulations, strengthens their credibility, promotes global acceptance, and assists innovation in *Bhasma* technology, effectively bridging the gap between ancient knowledge and modern nanomedicine.

This paper primarily focuses on the synthesis of *Yashad* and *Vanga Bhasmas* using the traditional method described in the Ayurvedic text "*Rasashastra*", their physicochemical characterization using modern analytical tools to assess structural features, and evaluation of their antibacterial activities against selected wound pathogens *B. subtilis* and *S. epidermidis* to validate their therapeutic potential.

2 Experimental procedures

2.1 Reagents

Raw zinc granules (Sigma-Aldrich; 99.9%), Raw tin granules (Sigma-Aldrich; 99.9%), Calcium hydroxide (Sigma-Aldrich; 99%), *Achyranthes aspera* powder, Aloe vera extract.

2.2 Preparation of *Yashad Bhasma* (YB) and *Vanga Bhasma* (VB)

Both *Bhasmas* were prepared following the traditional method described in the Ayurvedic text "*Rasashastra*, but using a muffle furnace for incineration instead of the traditional cow-dung-based *puta* heating system (Figure 1). Initially, 20 g of raw metal (zinc for YB and tin for VB) granules were repeatedly melted in an iron pan and quenched in 1 L of saturated lime water (pH = 11.3, experimentally measured using a digital pH meter) seven times, using fresh lime water in each cycle, until the metal appeared dull silver with some blackish coarse powder. The quenched metal was then heated with 2 g of *Achyranthes aspera* powder (*Apamarga churna*) under continuous stirring using an iron ladle until the metallic luster completely disappeared and only blackish powder remained. The resulting powder was collected at the center of the pan, covered with an earthen bowl, strongly heated to 250 °C for 90 min, and allowed to cool naturally. Subsequently, the powder was triturated with

fresh aqueous aloe-vera extract in a mortar for 45 min until converted into a paste. The paste was shaped into pellets of approximately 1 cm diameter and shade dried. The dried pellets were placed in a dry crucible and calcined in a muffle furnace at 350, 400, 450, 500, 550, 600, and 650 °C for 5 h at each temperature. The calcination process was carried out under ambient conditions (758 mmHg and 14 °C), with a heating rate of 100 °C min^{-1}, followed by natural cooling. The resulting greenish-yellow powder of YB and white powder of VB were finely ground and sieved through muslin cloth. The fine powders were labeled as SYB (Yashad Bhasma) and SVB (Vanga Bhasma), respectively, and stored separately in clean, dry glass vials.

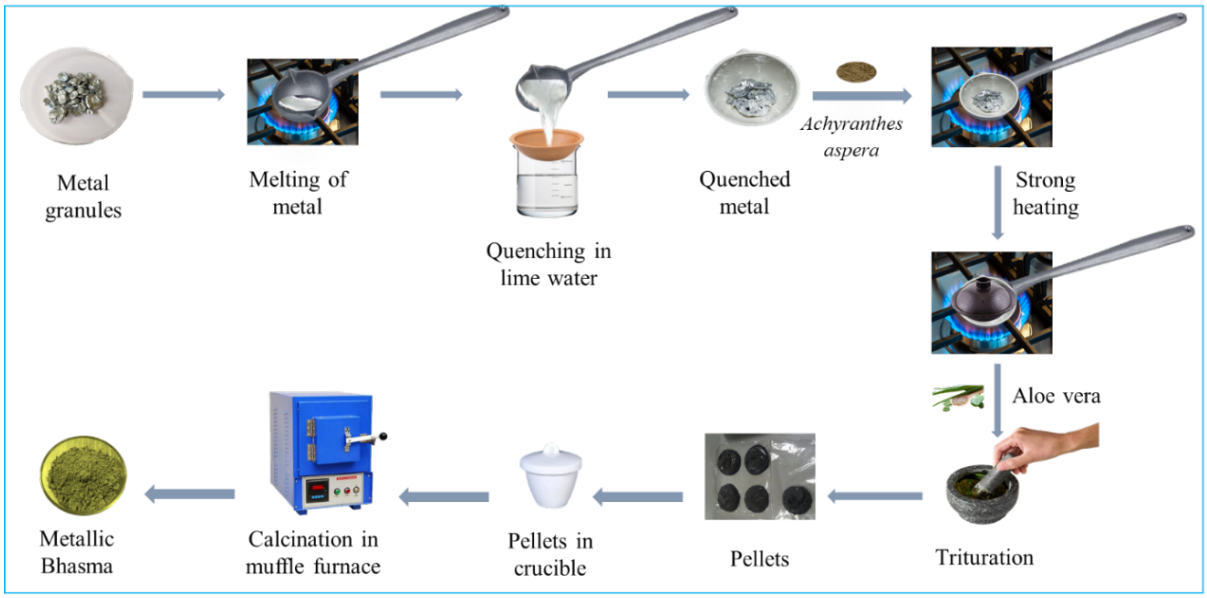

Figure 1: Schematic diagram showing the preparation of metallic *Bhasma*.

2.3 Characterization techniques

The following characterization of synthesized samples was performed to determine their optical and structural properties.

2.3.1 UV–Visible Spectroscopy

The optical absorption spectra of SYB and SVB samples were obtained by UV 1900 Shimadzu (USA) UV-Visible spectrophotometer. A total of 1 mg of the sample was dispersed in 10 mL of deionized water, sonicated for 5 minutes using an ultrasonic probe sonicator at a 25 Hz frequency with a 10-second on and 10-second off pulse cycle, and the spectrum was recorded in the range of $200 - 600$ nm. The data was also used to obtain a Tauc plot to calculate band gap energy.

The Tauc plot relation is expressed as [24]

$$(\alpha h\nu)^n = K(h\nu - E_g) \tag{1}$$

where α is the absorption coefficient, $h\nu$ is the incident photon energy, K is an energy-independent constant, E_g is the band gap energy, and n represents the nature of transitions, which can take values 2 (for direct allowed transition) or $\frac{1}{2}$ (for indirect allowed transition) [24].

In a Tauc plot, $h\nu$ (in eV) is plotted on the x-axis and $(\alpha h\nu)^n$ (in eV $cm^{-1})^n$ on the y-axis. The photon energy $h\nu$ is calculated using the relation [24]

$$h\nu = \frac{1240}{\text{Wavelength}} \tag{2}$$

The absorption coefficient α is calculated using the relation

$$\alpha = \frac{2.303 \times \text{Absorbance}}{\text{Path length}} \tag{3}$$

where the path length is taken as 1 cm.

A straight line was drawn through the linear part of the curve in the plot and elaborated towards the x-axis to get the band gap energy value.

2.3.2 Fourier Transform Infrared (FTIR) Spectroscopy

FTIR spectroscopy of the samples was performed with an IRAffinity–1S Shimadzu (Japan) FTIR spectrophotometer. Each sample was scanned (40 scans) from 400 to 4000 cm^{-1} at a resolution of 4 cm^{-1} in attenuated total reflection (ATR) mode.

2.3.3 X-ray Diffraction (XRD) Analysis

The crystal structure of the samples was investigated using a Bruker D8 Advance Eco P-XRD (Germany) system equipped with a Cu-Kα X-ray source of wavelength 1.541 Å. Samples were loaded on metal slides and placed inside the XRD analyzer. XRD patterns were recorded at a 2θ range of 20° to 80° and a scan rate of 6° per minute. The average crystallite sizes were calculated using the Debye–Scherrer equation

$$D = \frac{K\lambda}{\beta \cos\theta} \tag{4}$$

where D is the crystallite size, K is the Scherrer constant, λ is the X-ray wavelength, β is the peak full-width at half maximum (FWHM) in radians, and θ is the Bragg angle.

2.3.4 Raman Spectroscopy

Raman analysis of the samples was performed with LabRAM HR Evolution confocal Raman microscope (HORIBA France SAS). A pinch of sample was spread on a glass slide and scanned to observe Raman shift range for metal–oxygen bond vibrational modes from 100–1000 cm^{-1} at a resolution of 4 cm^{-1}. The data were collected and graphs were generated using Origin Pro software.

2.3.5 Field Emission Scanning Electron Microscopy (FESEM) and Energy Dispersive X-Ray (EDX) Analysis

Surface morphology and elemental composition were studied using a ZEISS Gemini SEM 500 (Germany) field emission scanning electron microscope (FESEM). A small amount of sample was sprinkled on a double–sided carbon tape mounted on aluminum stubs, gold sputtered and loaded on a movable stage of a microscope. The sample's surfaces were scanned at a magnification of 100,000× to obtain an electron image and elemental composition.

2.3.6 Field Emission Transmission Electron Microscopy (FETEM)

The microstructural analysis of the samples was performed with a JEOL JEM-2100F (Japan) field emission transmission electron microscope (FETEM). The sample was dispersed in deionized water and sonicated for 2 minutes. A drop of dispersion was deposited onto a carbon-coated copper grid (200 mesh size) of TEM and observed under magnification of 300,000×.

2.4 Antimicrobial Evaluation

The samples were evaluated for their antibacterial activity against Gram-positive wound pathogens Bacillus subtilis ATCC 6051 and Staphylococcus epidermidis ATCC 12228. The bacterial strains were obtained from Microbiologics Inc., 200 Cooper Avenue, North Saint Cloud, MN 56303. Colonies from 18–24–hour–old cultures of the test microorganisms were added to normal saline with subsequent vortexing until the turbidity of the suspension matched that of the 0.5 McFarland nephelometer standard to prepare inoculum suspensions and were used within 15 minutes of preparation. Test solutions of 100 mg mL^{-1} concentration were prepared by adding dimethyl sulfoxide (DMSO) to 1 g of the sample to make the final volume 10 mL followed by vortexing. The agar well diffusion technique [25] was used to assess antibacterial activity. Mueller – Hinton agar media was prepared and spread into sterile 90 mm Petri dishes. The inoculum suspensions were spread on the dried surface of the culture medium using a sterile swab. Three wells (two for the test samples and one for DMSO as a negative control) of 6 mm diameter were made on the inoculated plates, one each at the center of three of the four quadrants of the plates, using sterile cork borer. 50 µL of the test solutions and DMSO were dispensed into the wells using micropipettes. A suitable antimicrobial sensitivity disc, as a positive control, was placed at the center of the fourth quadrant of each of the inoculated Petri dishes. The inoculated plates were allowed to remain in the upright position for half an hour to allow the test solutions and negative control to diffuse into the media and then incubated in an inverted position at 35 °C for 18 hours. The zone of inhibition (ZOI) formed around the wells after incubation was measured using a vernier caliper.

The Broth Macro dilution method was used to determine minimum inhibitory concentration (MIC) and minimum bactericidal concentration (MBC) [26, 27]. Two–fold serial dilution of the test solution in Mueller–Hinton Broth (MBH) was done in 5 mL screw capped glass vials so that each vial contained 1 mL of the solutions of concentrations 50, 25, 12.5, 6.250, 3.125, 1.562, 0.781, 0.390, 0.195 and 0.097 mg mL^{-1}. Inoculum suspensions of the test microorganisms of density 5×105 cfu mL^{-1} were prepared in MBH and 1 mL of the suspensions was then added to each vial of the dilution series so that the dilution ratio of the test solutions and inoculum suspension becomes 1:2. Two vials of 1 mL pure MBH were also maintained. One of them was left uninoculated as a negative growth, while 1 mL of inoculum suspension was added to the other for positive growth. All the vials were then incubated at 35 °C for 18 hours. After incubation, the vials

were examined for growth as indicated by turbidity in comparison to the negative growth vial. 0.005 mL of the MIC vial contents was drawn using a calibrated loop and was sub-cultured on fresh nutrient agar media at the same temperature and duration as for the MIC vials. MBC was interpreted as the lowest concentration showing no visible colony formation on agar plates after incubation, indicating complete bactericidal activity.

3 Results and discussion

3.1 UV-visible spectroscopy

While commercial *Yashad* and *Vanga Bhasma* showed UV-visible absorption peaks at 347 nm and 290 nm, respectively [28], the UV–visible spectra revealed a distinct surface plasmon resonance (SPR) absorption peak at 374 nm for SYB (Figure 2(A)) and 310 nm for SVB (Figure 2(C)). These findings are consistent with previous reports on green-synthesized ZnO nanoparticles exhibiting SPR absorption at 374 nm [29] and biosynthesized SnO_2 nanoparticles showing an absorption band around 275 nm [30]. The optical direct band gap energies, estimated using the Tauc plots, were determined to be 3.8 eV for SYB (Figure 2(B)) and 3.33 eV for SVB (Figure 2(D)). The observed SPR peaks and corresponding band gap energies are attributed to the intrinsic band-gap transitions of ZnO and SnO_2 arising from electron excitations from the O^{2-} (2p) valence band to Zn (3d) and Sn (3d) conduction bands, respectively, confirming the presence of ZnO and SnO_2 nanoparticles [29,30].

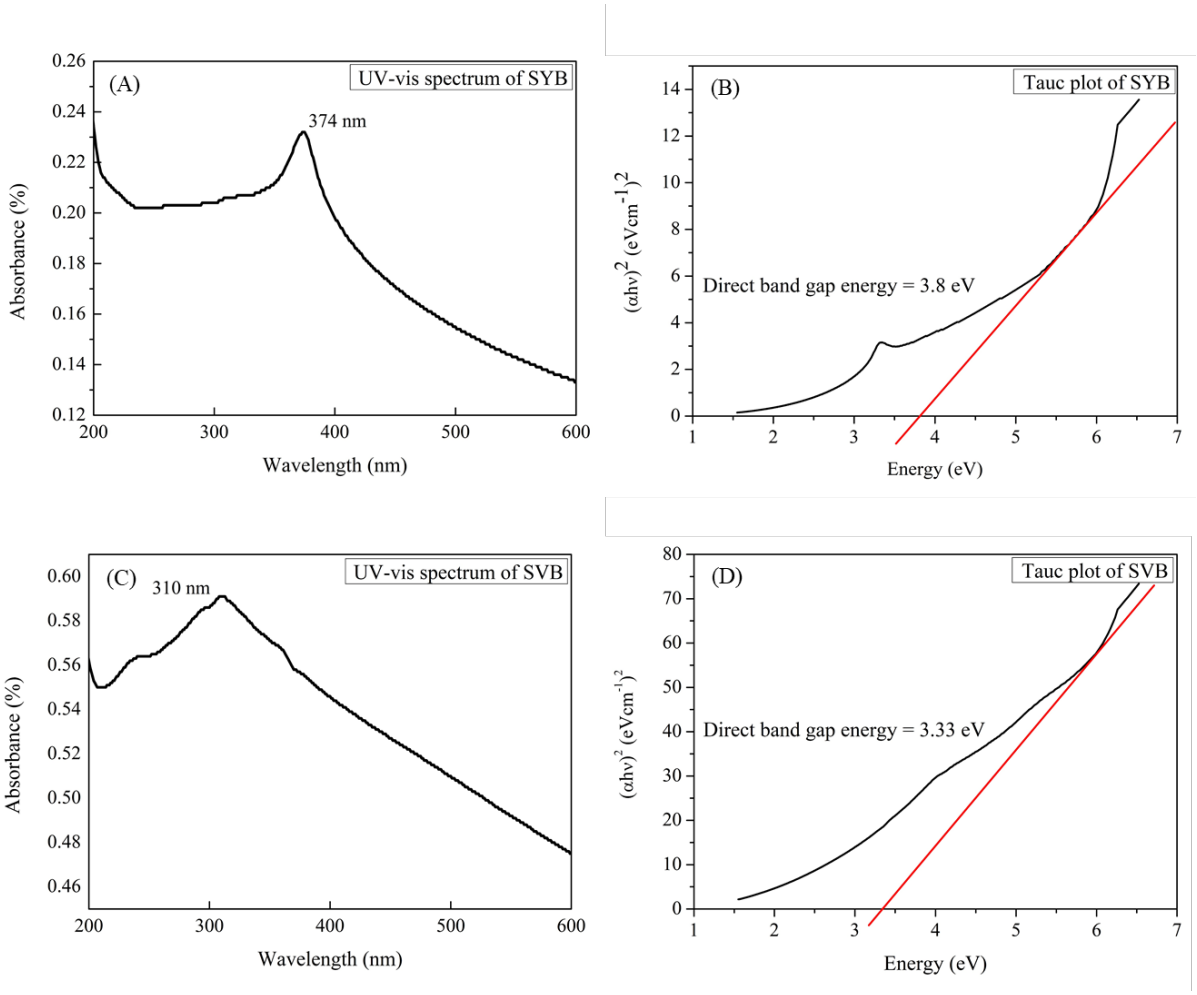

Figure 2: UV–visible spectrum and corresponding Tauc plot of SYB (A and B) and SVB (C and D).

3.2 FTIR spectroscopy

In the FTIR spectrum of SYB (Figure 3(A)), characteristic absorption bands were detected at approximately 3865, 3721, 2981, 2323, 1544, 1070, and 421 cm^{-1}. Consistent with the previous literature [28,29,31], the bands near 3865 and 3721 cm^{-1} correspond to O–H stretching vibrations of phenolic hydroxyl groups, while the weak band at 2981 cm^{-1} is attributed to C–H stretching vibrations of alkanes. The absorption near 2323 cm^{-1} may be

attributed to primary and secondary amine groups; however, this region is also commonly associated with CO_2-related absorption bands, whereas the band at 1544 cm^{-1} is assigned to N–O asymmetric stretching of nitro compounds. The peak observed at 1070 cm^{-1} corresponds to C–OH stretching vibrations, while the prominent peak at 420 cm^{-1} is associated with Zn–O stretching vibrations [29]. These findings suggest the presence of metabolites such as alkaloids, flavonoids, polyphenols, amino groups and carboxylic acids adsorbed on ZnO nanoparticle surface.

Similarly, the FTIR spectrum of SVB (Figure 3(B)) displayed absorption bands around 1449, 1114, 605 and 459 cm^{-1}. In agreement with the previous literature [28,30], the band at 1449 cm^{-1} corresponds to C==C stretching of alkenes, while the absorption at 605 cm^{-1} is assigned to O–Sn–O stretching vibrations. The peak at 459 cm^{-1} represents Cu–O stretching, indicating trace CuO nanoparticle impurities [28, 30, 31].

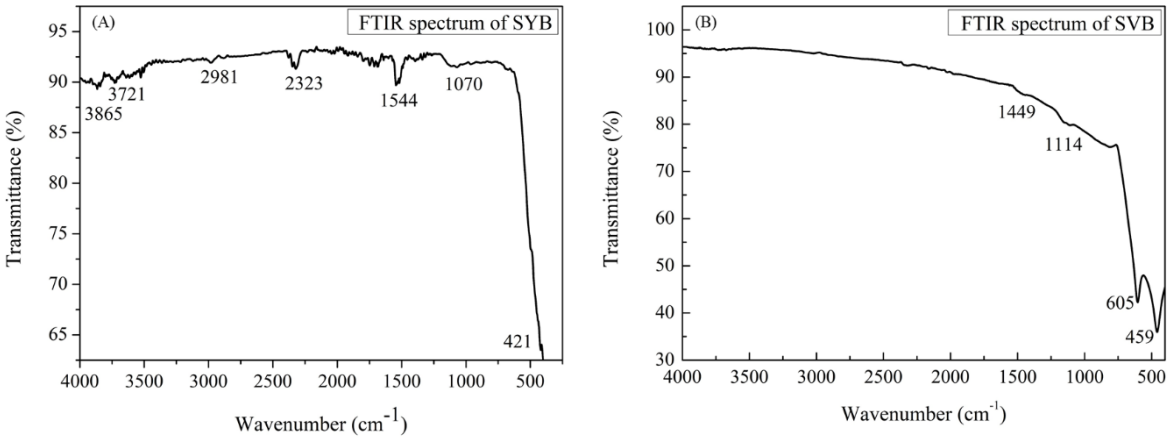

Figure 3: FTIR spectra of SYB (A) and SVB (B).

3.3 XRD analysis

The XRD pattern of SYB (Figure 4(A)) revealed peaks at 2θ values of 32.0°, 34.6°, 36.4°, 47.7°, 56.7°, 63.0° and 68.1° corresponding to the diffraction from Miller indices planes (100), (002), (101), (102), (110), (103) and (112), respectively. The planes match the hexagonal phase having a wurtzite structure of ZnO (JCPDS card no.: 89–7102). This pattern is also in agreement with the XRD pattern of green synthesized ZnO nanoparticles and *Yashad Bhasma* reported in the earlier literature [10,29,32]. The average crystallite size of SYB samples, calculated using Scherrer's equation ($D = K\lambda/\beta \cos\theta$), was 20.23 nm (Table 1).

Table 1: Calculation of average crystallite size of SYB using Scherrer's equation

K	λ	2θ	FWHM	β (radian)	Crystallite size (D)	Average D (nm)
0.94	0.15406	32.0	0.4	0.006981	21.58	20.23
0.94	0.15406	34.6	0.4	0.006981	21.73	
0.94	0.15406	36.4	0.4	0.006981	21.84	
0.94	0.15406	47.7	0.5	0.008727	18.14	
0.94	0.15406	56.7	0.5	0.008727	18.86	
0.94	0.15406	63.0	0.5	0.008727	19.46	
0.94	0.15406	68.1	0.5	0.008727	20.03	

Similarly, the XRD pattern of SVB (Figure 4(B)) revealed peaks at 2θ values of 26.6°, 33.9°, 38.0°, 51.8°, 54.8°, 61.9°, 64.8° and 66.0° corresponding to the diffraction from Miller indices planes (110), (101), (200), (211), (220), (311), (301) and (321) planes respectively. The diffraction pattern corresponds to the tetragonal rutile structure of SnO_2 nanoparticles (JCPDS card no.: 96–210–4744). This pattern is consistent to the XRD pattern of biosynthesized SnO_2 nanoparticles and vanga bhasma reported in the previous literature [10,30]. The average crystallite size of SVB samples, calculated using Scherrer's equation, was 38.17 nm (Table 2).

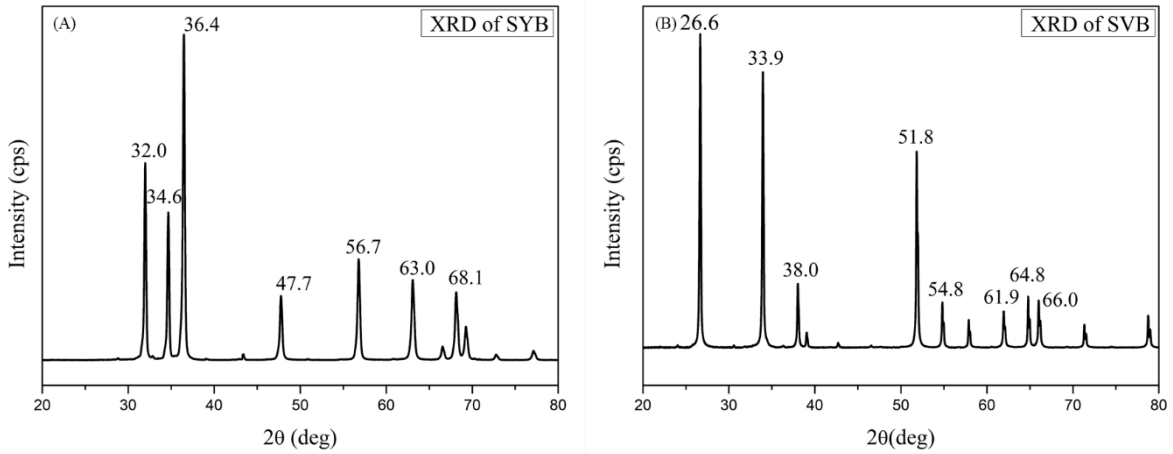

Figure 4: X–Ray Diffractogram of SYB (A) and SVB (B).

Table 2: Calculation of average crystallite size of SVB using Scherrer's equation

K	**λ**	**2θ**	**FWHM**	**β** (radian)	**Crystallite size (D)**	**Average D (nm)**
0.94	0.15406	26.6	0.2	0.003491	42.63	38.17
0.94	0.15406	33.9	0.2	0.003491	43.37	
0.94	0.15406	38.0	0.2	0.003491	43.88	
0.94	0.15406	51.8	0.3	0.005236	30.75	
0.94	0.15406	54.8	0.2	0.003491	46.73	
0.94	0.15406	61.9	0.3	0.005236	32.25	
0.94	0.15406	64.8	0.3	0.005236	32.76	
0.94	0.15406	66.0	0.3	0.005236	32.98	

3.4 Raman spectroscopy

The Raman spectrum of SYB (Figure 5(A)) exhibited prominent and sharp peaks at 198.6, 326.8, 433.6, and 569.2 cm^{-1}, indicative of its crystalline nature. As reported in the previous literature, the peak at 433.6 cm^{-1} corresponds to the E_2 (high) mode of ZnO, a characteristic feature of the wurtzite ZnO lattice. The peaks at 198.6 and 326.8 cm^{-1} are attributed to low–energy stretching and bending vibrational modes of Zn–O lattice, whereas the intense peak at 569.2 cm^{-1} is assigned to the E_1(LO) mode, suggesting the presence of oxygen vacancies and associated structural imperfections [33].

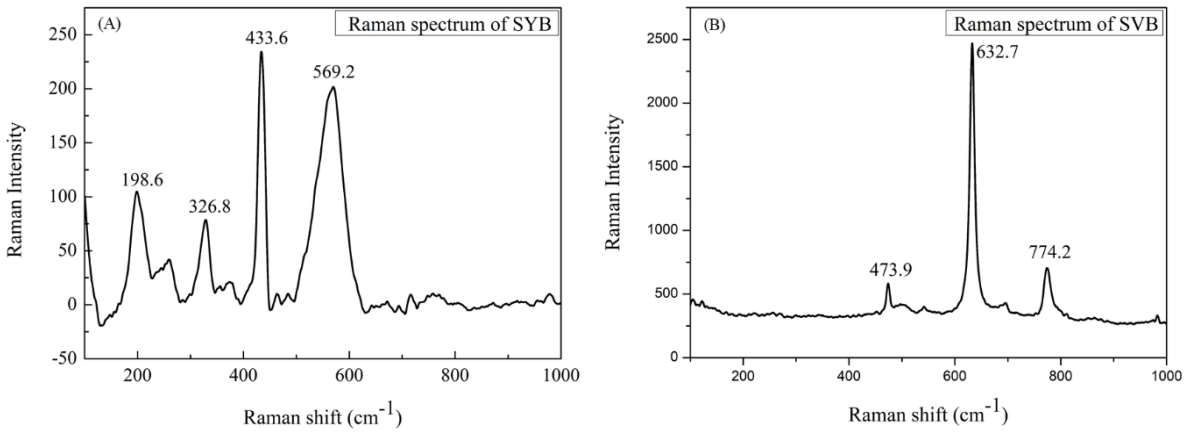

Figure 5: Raman spectra of SYB (A) and SVB (B).

Similarly, the Raman spectrum of SVB (Figure 5(B)) displayed prominent peaks at 473.9, 632.7 and 774.2 cm^{-1}, also confirming its crystalline nature. Consistent with the previous literature [34], these peaks are assigned to E_g, A_{1g} and B_{2g} vibrational modes of SnO_2, which are characteristic of the tetragonal rutile SnO_2 structure.

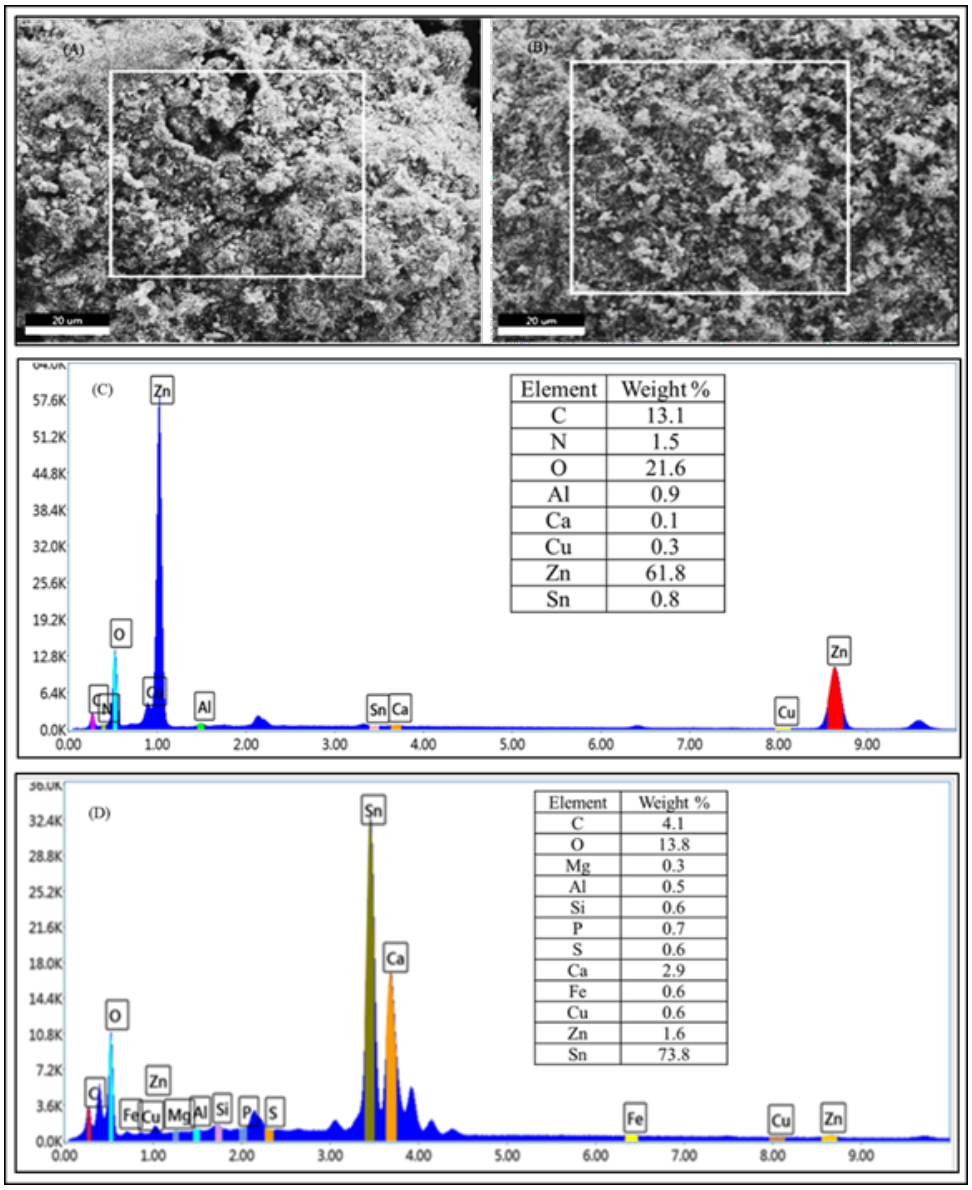

Figure 6: FESEM image of SYB (A) and SVB (B), and EDX report of SYB (C) and SVB (D).

3.5 FESEM and EDX analysis

As depicted in Figures 6(A) and (B), the SEM–EDX report of SYB demonstrated rough texture, granular and porous morphology with agglomerated structure, consisting of 61.8% zinc and 21.6% oxygen along with 13% carbon and traces of nitrogen, aluminum, calcium, copper, and tin. This result is in good agreement with XRD and Raman results of the SYB sample, which confirms the presence of crystallite zinc oxide particles in the sample. Similarly, the SEM–EDX report of SVB (Figure 6(C) and (D) also displayed rough texture and porous morphology with agglomerated structure, consisting of 73.8% tin and 13.8% oxygen along with 4.1% carbon, 2.9% calcium and traces of magnesium, aluminum, silicon, phosphorus, sulphur, iron, copper and zinc. This result is in good agreement with XRD and Raman results of SVB sample, confirming the presence of crystalline tin oxide particles.

3.6 FETEM analysis

As shown in Figures 7(A) and (B), the FETEM image of SYB reveals a circular agglomeration of ir-

regularly shaped particles with a size ranging from 15.04 to 25.73 nm. The average particle size distribution of SYB is 21.3 nm. Similarly, FETEM image of SVB (Figure 7(C) and (D)) shows a flower-like agglomeration of irregularly shaped particles with particle size ranging from 31.72–52.31 nm. The average particle size distribution of SVB is 38.5 nm. The close agreement between TEM particle sizes and XRD crystallite sizes of SYB and SVB indicates that the particles are predominantly single crystallites, with minimal agglomeration at the level of primary particles.

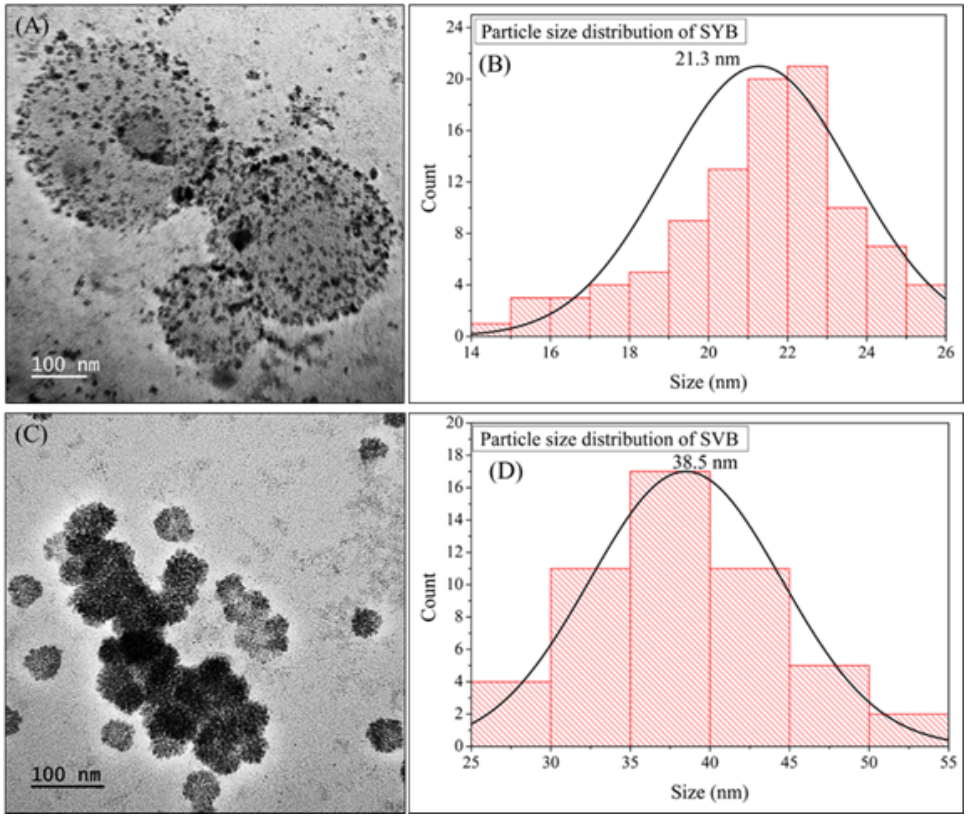

Figure 7: FETEM image and size distribution pattern of SYB (A and B) and SVB (C and D).

3.7 Antimicrobial analysis

The inhibition zones produced by SYB and SVB against wound-associated pathogens, Bacillus subtilis and Staphylococcus epidermidis, at a test concentration of 100 mg.mL^{-1} are displayed in Figure 8. SYB produced an inhibition zone of size 11.00±0.3 mm and 11.34±0.3 mm against B. subtilis and S. epidermis, respectively. The inhibition zone observed for SYB indicates its significant antibacterial potency, which can be attributed to its small size, high surface–to–volume ratio, and the presence of organic components. The release of Zn^{2+} ions and generation of reactive oxygen species (ROS) such as O_2^- by SYB are likely to damage bacterial cell membranes and disrupt bacterial metabolism [35]. Although *Vanga Bhasma* is reported to show antimicrobial effect against bacteria such as *S. aureus* and *E. coli* [14], SVB in this research did not show any activity against *B. subtilis* and *S. epidermidis*. It may be likely due to inadequate incineration during its preparation or inadequate concentration of the test solution prepared during the antimicrobial test. The MIC of the samples against both pathogens could not be interpreted due to the turbidity of the test solutions, while MBC values provide significant insight into the bactericidal efficacy of the samples. SYB displayed MBC values ranging between 12.5–25 mg.mL^{-1} for both pathogens, which can be attributed to the presence of ZnO nanoparticles and are comparable to the reported MBC values of ZnO nanoparticles towards *B. subtilis* (19.53 mg.mL^{-1}) [36] and *S. epidermidis* (7.81 mg.mL^{-1}) [37].

4 Conclusion

Yashad Bhasma (Zinc calx) and *Vanga Bhasma* (Tin calx) were prepared by following traditional Ayurvedic processing techniques mentioned in "Rasashastra", and their physicochemical and antimicrobial properties were evaluated using modern analytical tools. UV–visible spectroscopy revealed

surface plasmon resonance peaks at 374 nm for YB and 310 nm for VB, with optical band gap energies of 3.8 and 3.33 eV, respectively. FTIR and Raman spectra confirmed the presence of metal-oxygen bonds along with organic groups in both the *Bhasmas*.

XRD analyses confirmed the crystalline wurtzite ZnO structure of YB and the rutile SnO_2 structure of VB. SEM–EDX micrographs of YB revealed rough, granular, and porous agglomerates rich in ZnO with 61.8% zinc and 21.6% oxygen, along with 13% carbon, while those of VB showed porous agglomerates of SnO_2 with 73.8% tin and 13.8% oxygen, along with 4.1% carbon. TEM images showed circular agglomerates (~21.3 nm) in YB and flower–like agglomerates (~38.5 nm) in VB. These results elucidate that the traditional Ayurvedic processing techniques are not only efficient at reducing the particle size to the nanoscale level but also transform raw metal to metal oxide nanoparticles. Antimicrobial assays demonstrated notable inhibitory activity of YB, showing stronger effects against wound pathogens *B. subtilis* and *S. epidermidis*, supporting its potential relevance in biomedical sectors. However, further detailed in vitro and in vivo studies are required to validate their therapeutic applicability.

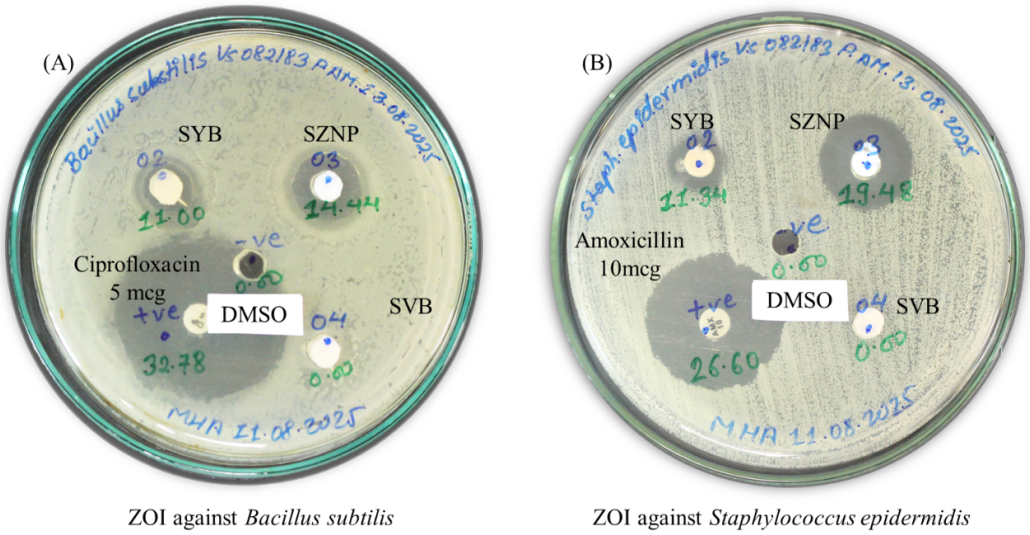

ZOI against *Bacillus subtilis* ZOI against *Staphylococcus epidermidis*

Figure 8: Antimicrobial action of SYB and SVB towards *B. subtilis* (A) and *S. epidermidis (B)*.

Acknowledgements

We thank Tribhuvan University, Bhaktapur Multiple Campus, Bhaktapur, Nepal for providing study leave for BR; North East Centre for Biological Sciences and Healthcare Engineering (NECBH), Indian Institute of Technology (IIT) Guwahati for laboratory support and Department of Biotechnology (DBT), Government of India for supporting the research (Project No. BT/NER/143/SP44675/2023); and Department of Plant Resources, Government of Nepal supporting this work through biological tests. We further thank the Ministry of Education Science and Technology for supporting the project "Development of Polymeric Liquid Bandage Infused with *Yashad Bhasma* and Zinc Oxide Nanoparticles for Enhanced Wound Healing".

References

[1] Pal D, et al. Bhasma: The ancient Indian nanomedicine. Journal of Advanced Pharmaceutical Technology and Research. 2014;5:4.

[2] Jawale KE, Rakibe A. Concept of Bhasma, their Preparation and Significance in Rasashastra. Himalayan Journal of Health Sciences. 2025:9-11.

[3] Pal S. The Ayurvedic Bhasma: The Ancient Science of Nanomedicine. Recent Patents on Nanomedicine. 2015;5:12-8.

[4] Joshi N, et al. Toxicity study of Lauha Bhasma (calcined iron) in albino rats. Ancient Science of Life. 2016;35:159.

[5] Jagtap CY, et al. Acute and Subchronic Toxicity Study of Tamra Bhasma (Incinerated Copper) prepared from Ashodhita (Unpurified) and Shodhita (Purified) Tamra in

Rats. Indian Journal of Pharmaceutical Sciences. 2013;75:346.

[6] Liu J, et al. Chemical Compositions of Metals in Bhasmas and Tibetan Zuotai Are a Major Determinant of Their Therapeutic Effects and Toxicity. Evidence-Based Complementary and Alternative Medicine. 2019;2019:1697804.

[7] Gadad GG, et al. Comparative Pharmaceutico-Analytical Study of Classical, Yashada Bhasma and Potentiated Yashada Bhasma. Frontiers in Health Informatics. 2024;13:486-96.

[8] Patil S, Chaudhary AK. Characterization of yashad bhasma (Zinc calx) and establishment of the importance of shodhan (purification). Indian Journal of Natural Products and Resources. 2021;12:291-9.

[9] Pareek A, Bhatnagar N. Physico-chemical characterization of traditionally prepared Yashada bhasma. Journal of Ayurveda and Integrative Medicine. 2020;11:228-35.

[10] Asmita W, et al. Pharmaceutics and standardization of Ayurvedic Bhasma: A comprehensive review. Journal of Drug Research in Ayurvedic Sciences. 2025;10:4-21.

[11] Kale B, Rajurkar N. Synthesis and characterization of Vanga bhasma. Journal of Ayurveda and Integrative Medicine. 2019;10:111-8.

[12] Devi P. Pharmaceutical and analytical studies on Vanga Bhasma: an updated review. Journal of Ayurvedic and Herbal Medicine. 2021;7:49-55.

[13] Baruah H, et al. Therapeutic uses of Vanga bhasma: A critical review. International Journal of Research in Ayurveda and Pharmacy. 2014;5:566-70.

[14] Belge R, et al. Analytical and antimicrobial study of Vanga Bhasma with special reference to Ayurved Prakash. Journal of Ayurveda and Integrated Medical Sciences. 2021;6:33-43.

[15] Nille GC, et al. Characterization and potential novel applications of zinc-based traditional medicine, Yashad Bhasma. Journal of Ayurveda and Integrative Medicine. 2025;16:101188.

[16] Verma SK, Yadav S. Analysis of Physicochemical Properties and Antimicrobial Activity of Some Traditional Indian Ayurvedic Bhasmas. World Journal of Pharmaceutical Research. 2014;3045:1931-46.

[17] Adhikari R. Ayurvedic Bhasmas: Overview on Nanomaterialistic Aspects, Applications, and Perspectives. In: Advances in Experimental Medicine and Biology. vol. 807; 2014. p. 23-32.

[18] Kumar A, et al. Bhasmas: Unique Ayurvedic metallic-herbal preparations, chemical characterization. Biological Trace Element Research. 2006;109:231-54.

[19] Hirudkar VN, et al. Bhasma Therapy: Bridging Ayurveda'S Rasa Shastra with Modern Nanomedicine. World Journal of Pharmaceutical and Medical Research. 2015;10:346-8.

[20] Kulkarni SS. Bhasma and Nano Medicine. International Research Journal of Pharmacy. 2016;4:10-6.

[21] Valikarimwala M, et al. Applications of Nanotechnology in Ayurveda: A Review. Research and Reviews in Biotechnology and Biosciences. 2021;8:163-9.

[22] Sreelakshmi S, et al. Ayurvedic bhasma and synthesized nanoparticles: A comparative review. In: Materials Today: Proceedings. Elsevier Ltd; 2020. .

[23] Chavhan SA, Shrikhande VN. A Comprehensive Review on Bhasma and Herbomineral Formulation in Ayurveda. International Journal of Advanced Research, Ideas and Innovations in Technology. 2020;6:1511-9.

[24] Harynski L, et al. A facile method for Tauc exponent and corresponding electronic transitions determination in semiconductors directly from UV–Vis spectroscopy data. Optical Materials. 2022;127:112205.

[25] Perez C, et al. An antibiotic assay by the agar well diffusion method. Acta Biologica et Medica Experimentalis. 1990;15:113-5.

[26] Sykes JE, Rankin SC. Isolation and Identification of Aerobic and Anaerobic Bacteria. 2013:17-28.

[27] Balouiri M, et al. Methods for in vitro evaluating antimicrobial activity: A review. Journal of Pharmaceutical Analysis. 2016;6:71-9.

[28] Rajchal B, et al. Microstructural Investigation of Commercial Ayurvedic Bhasma Samples by Optical, UV-visible and FTIR Analyses. Advanced Materials Letters. 2025;16:2502-1777.

[29] Patil BN, Taranath TC. Limonia acidissima L. leaf mediated synthesis of zinc oxide nanoparticles: A potent tool against Mycobacterium tuberculosis. International Journal of Mycobacteriology. 2016;5:197-204.

[30] Narasaiah BP, et al. Green Biosynthesis of Tin Oxide Nanomaterials Mediated by Agro-Waste Cotton Boll Peel Extracts for the Remediation of Environmental Pollutant Dyes. ACS Omega. 2022;7:15423-38.

[31] Hussain SMB, et al. Green synthesis of zinc oxide nanoparticles using Pulicaria undulata extract: Evaluation of antibacterial and larvicidal efficacy against Aedes aegypti. Parasite Epidemiology and Control. 2026;32.

[32] Savrikar S, et al. Comparative study of Marketed samples of Yeshada Bhasma, An Ayurvedic Medicinal Preparation based on XRF, XRD and Particle Size Analysis. Annals of Ayurvedic Medicine. 2026;15:97.

[33] Sharma A, et al. Effect of surface groups on the luminescence property of ZnO nanoparticles synthesized by sol-gel route. Surface Science. 2012;606.

[34] Diéguez A, et al. The complete Raman spectrum of nanometric SnO_2 particles. Journal of Applied Physics. 2001;90:1550-7.

[35] Wang L, et al. The antimicrobial activity of nanoparticles: present situation and prospects for the future. International Journal of Nanomedicine. 2017;12:1227-49.

[36] Jamal A, et al. Evaluation of Antimicrobial Activity of ZnO Nanoparticles against Foodborne Pathogens. International Journal of Current Microbiology and Applied Sciences. 2019;8:2000-25.

[37] Anbukkarasi V, et al. Antimicrobial Activity of Green Synthesized Zinc Oxide Nanoparticles from Embica Officinalis. International Journal of Pharmaceutical Sciences Review and Research. 2015;33:110-5.